Int. J. Electrochem. Sci., 8 **(2013)** 1366 - 1381

International Journal of
ELECTROCHEMICAL
SCIENCE
www.electrochemsci.org

Facile Synthesis of Mesoporous CuO Nanoribbons for Electrochemical Capacitors Applications

Yu Xin Zhang[1,*], *Ming Huang*[1], *Min Kuang*[1], *Chuan Pu Liu*[1,*], *Jian Liang Tan*[2], *Meng Dong*[1], *Yuan Yuan*[1,3], *Xiao Li Zhao*[1], *Zhongquan Wen*[4]

[1] College of Material Science and Engineering, Chongqing University, Chongqing, 400045, China
[2] National University of Singapore, 10 Kent Ridge Crescent, 119260, Singapore
[3] State Key Laboratory of Power Transmission Equipment & System Security and New Technology, Chongqing University, Chongqing 400045, China
[4] Defense Key Disciplines Lab of Novel Micro-nano Devices and System Technology, Chongqing University, Chongqing, 400045, China
[*]E-mail: zhangyx_cqu@163.com, liuchuanpu@163.com

Received: 22 November 2012 / *Accepted:* 17 December 2012 / *Published:* 1 January 2013

Mesoporous ribbon-like CuO has been synthesized via a facile and scaleable wet-chemical method, accompanied with tetraoctylammonium bromide (TOAB) as a soft template under ambient condition. Characterizations studies including x-ray diffraction spectroscopy (XRD), fourier transform infrared spectroscopy (FTIR), field emission scanning electron microscopy (FESEM), and high-resolution-transmission electron microscopy (HRTEM) were applied to investigate the structure and morphology of the as-synthesized CuO. Further physical characterizations revealed that CuO nanoribbons owned a comparatively higher specific surface area with typical mesoporous appearance. The electrochemical properties of the mesoporous CuO were elucidated by cyclic voltammograms, galvanostatic charge-discharge tests in 6 M KOH electrolyte. Electrochemical data analysis demonstrated that as-synthesized CuO nanoribbons exhibited a higher specific capacitance of 137 F g^{-1} and stable cycling performance of only 12% capacitance loss after 500 cycles. These results suggest that the low-cost CuO electrode is a promising candidate for high-performance electrochemical capacitors.

Keywords: CuO, ribbon-like, soft template, mesoporous, electrochemical properties

1. INTRODUCTION

Supercapacitors also known as electrochemical capacitors, are electrochemical energy storage devices for applications in energy back-up systems, camera flash equipment, consumer portable devices, and electrical/hybrid automobiles [1-4]. In recent years, much research effort has been directed to develop nanoarchitectures of materials for supercapacitors by virtue of their unique

properties such as high specific surface area, shorter ion diffusion, and electrochemical activity [5-9]. The capacitance in an electrochemical capacitor can arise from the charging and discharging of the electrical double layers or from faradic redox reactions called as pseudocapacitance. Carbon (e.g., activated carbon, carbon nanotube, and graphene) is recognized as a promising material for electrochemical double layer capacitors because of its low cost [7, 10], but it exhibits a low specific capacity. RuO_2 and IrO_2 of noble metal oxide materials were used as pseudocapacitive electrode materials with remarkable performance [11, 12], however, the high cost of hydrous ruthenium oxide and iridium oxide hindered their wide application. Accordingly, more and more interest has been recently focused on those cheap transition metal oxides, such as nickel oxide (NiO) [13], cobalt oxide (Co_3O_4) [14], vanadium oxide (V_2O_5) [15], manganese oxide (MnO_2) [16], and copper oxide (CuO) [17]. However, the small micropores of nanostructures are not suitable for the diffusion of solvated ions, especially when a large loading current density is employed. Therefore, total surface area cannot be utilized efficiently, resulting in undesirable capacitive performance. While, the mesopores (>2 nm) are favorable for ion diffusion with high speed in such pores even at high loading current density. Then it is still a challenge to synthesize transition metal oxides nanostructures for supercapacitors with mesoporous morphology.

Among the transition metal oxides, mesoporous CuO is noteworthy to explore as a promising candidate due to its low cost, abundant resources, non-toxicity, chemically stable, and easy preparation in diverse shapes of nano-sized dimension. Nowadays, many methods have been developed to synthesize various CuO nanostructures [18-23], and the supercapacitance behavior of CuO has attracted more and more research interest. For instance, Patake et al. [24] synthesized the porous amorphous copper oxide thin films which exhibited a specific capacitance of 36 F g^{-1} in 1 M Na_2SO_4 electrolyte. Dubal et al. [25]have prepared copper oxide multilayer nanosheets thin films with a specific capacitance of 43 F g^{-1} in 1 M Na_2SO_4 electrolyte. Zhang et al. [26, 27] reported that CuO with flower-like nanostructures displayed a specific capacitance of 133.6 F g^{-1} in 6 M KOH electrolyte, which is about three-fold higher than commercial CuO powder, however, the specific capacitance of CuO is still lower than other transition metal oxides and exhibited unstable cycling performances. Very recently, Wang et al. [28] have reported the synthesis of CuO nanosheet arrays directly grown onto nickel foam with higher specific capacitance of 569 F g^{-1}, whereas the method employed is relatively complicated and low yield. To the best of our knowledge, mesoporous CuO nanoribbons prepared by surfactant-assisted method at one step with a reasonable specific capacitance and better cycling performance have seldomly been reported.

Herein, we report a facile, cost-effective and scaleable synthesis approach to prepared porous CuO nanoribbons in the presence of tetraoctylammonium bromide (TOAB) at room temperature. The morphology, structure and electrochemical properties of the CuO nanoribbons were investigated. Furthermore, a possible growth mechanism of CuO nanocrystals was discussed and the investigations on TOAB roles were also carried out. Remarkably, the electrode of CuO nanoribbons exhibited promising specific capacitance and excellent capacitance retention during cycling.

2. EXPERIMENTAL

2.1 Materials

Copper nitrate ($Cu(NO_3)_2 \cdot 3H_2O$), sodium hydrate (NaOH), potassium hydrate (KOH), ammonia ($NH_3 \cdot H_2O$), ethanol (C_2H_5OH), tetraoctylammonium bromide (TOAB), sodium nitrate ($NaNO_3$), polyvinylidene fluoride (PVDF) and solvents used in this work were purchased from Alfa Aesar. The entire chemicals were of analytical purity and used without any further purification.

2.2 Synthesis of mesoporous CuO nanostructures

The CuO nanoribbons were prepared with surfactant-assisted wet-chemical method. Typically, 20 mL aqueous solution of $Cu(NO_3)_2 \cdot 3H_2O$ (0.05 M) was mixed with varying amounts (10, 20, 40 mL) of TOAB ethanol solution (0.05 M) in a round-bottom flask at room temperature and kept vigorous stirring for 5 min. Afterwards, aqueous NaOH solution (10 mL, 1.00 M) was dropwisely added into the mixture and the mixture was kept vigorous stirring for 1.5 h. The resulting brownish black precipitate was separated, centrifuged, washed with distilled water and ethanol for several times, and then dried at 60 ^{o}C overnight. The product prepared with 20 mL TOAB was signed as sample A, and the one prepared with 40 mL TOAB was signed as sample B.

As a complementary study, the CuO microspheres were prepared a hydrothermal route [29]. In a typical synthesis, 15 mL of $Cu(NO_3)_2 \cdot 3H_2O$ ethanol solution (1.00 M) was added with 15 mL of ammonia solution (28%), followed by an addition of 5 mL of aqueous NaOH (1.00 M) and 1 g of solid $NaNO_3$. The solution mixture was transferred to a Teflon-lined stainless steel autoclave, which was then heated at 100 °C for 24 h in an electric oven. After reaction, the autoclave was cooled in tap water, and CuO products were centrifuged, washed with distilled water and ethanol for several times, and then dried at 60 ^{o}C overnight. The product was signed as sample C.

2.3 Characterization

The crystallographic information and chemical composition of as-prepared products were established by powder X-ray diffraction (XRD, D/max 1200, Cu Kα) and Fourier transform infrared spectroscopy (FTIR, Nicolet 5DXC), thermogravimetric analyzer-differential scanning calorimeter (TGA-DSC, NETZSCH STA 449C). The structural and morphological investigations of the CuO nanostructures were carried out with High-resolution transmission electron microscopy (HRTEM, ZEISS LIBRA 200), and Field emission scanning electron microscopy (FESEM, FEI NOVA 400). Nitrogen adsorption-desorption isotherms were measured at 77K with micrometritics ASAP 2020 sorptometer. The specific surface area was calculated with the Brunauer-Emmett-Teller (BET) equation, and the pore size distributions were calculated from the adsorption curve by the Barrett–Joyner–Halenda (BJH) method.

2.4 Electrochemical measurements

The electrochemical measurements including cyclic voltammetry (CV) and galvanostatic charge-discharge (GC) tests were performed by using a CHI 660D electrochemical workstation under ambient conditions. In a typical electrochemical measurement, a three-electrode cell system was composed of CuO powders electrode as the working electrode, a platinum plate as the counter electrode, and a saturated calomel electrode as the reference electrode. The working electrode was fabricated by mixing the 70 wt% as-prepared CuO with 20 wt% acetylene black and 10 wt% polyvinylidene fluoride (PVDF), and then a slurry of above mixture was painted onto the foamed nickel as a current collector. The coated mesh was dried at 120 ^{o}C in vacuum cabinet overnight to remove the solvent and water.

The capacitive behaviors of the CuO were characterized by cyclic voltammetry (CV) in 6 M KOH electrolyte at room temperature. CV measurements were performed on the three-electrode cells in the voltage window between 0 and 0.4 V at different scan rates. Galvanostatic charge-discharge experiments were performed with different current densities to reflect the rate ability.

3. RESULTS AND DISCUSSION

3.1 Structure and morphology

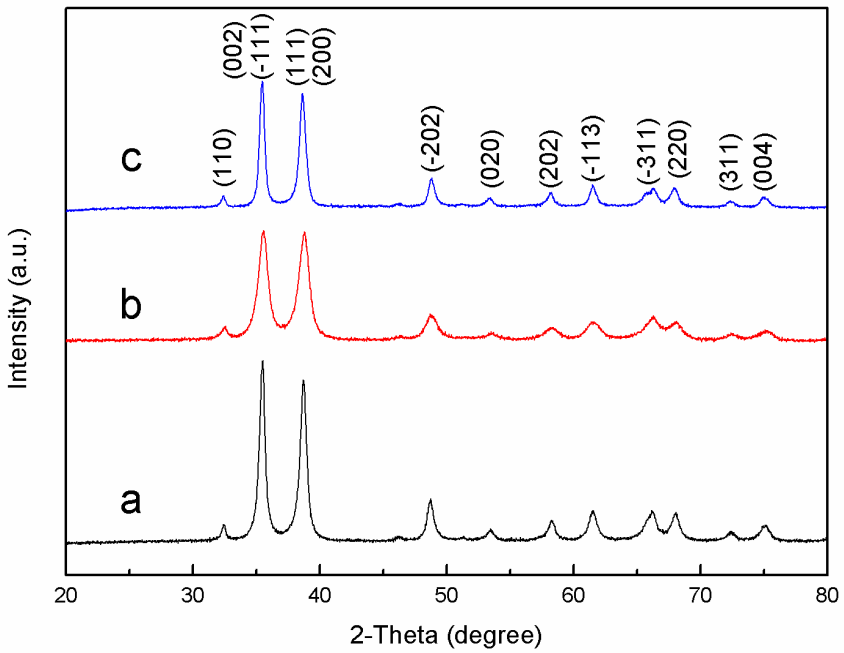

Figure 1. XRD patterns of different mesoporous CuO nanocrystallines: a) prepared with $Cu(NO_3)_2$/TOAB=1:1 at room temperature, and b) prepared with $Cu(NO_3)_2$/TOAB=1:2 at room temperature, and c) prepared with $Cu(NO_3)_2$/NaOH=3:1 with 15 mL of ammonia solution at 100 ^{o}C for 24 h.

Fig.1 presents the composition and crystallite phase purity of the as-prepared mesoporous CuO nanostructures (sample A, B and C), examined by powder XRD, which confirmed a high degree of crystallinity with all reflections indexed to the monoclinic CuO (JCPDS card no. 05-0661, a = 4.684 Å, b = 3.425 Å, c =5.129 Å and β = 99.47^o), similar to the previous literature [30, 31], and XRD patterns of the sample prepared with 10 mL TOAB is the same as the above (See Supplementary Information, SI-1). The dominant peaks located at 2θ values between 20° and 80° clearly indicate that the CuO product is a pure phase, while no characteristic peaks of impurities such as $Cu(OH)_2$ and Cu_2O were detected.

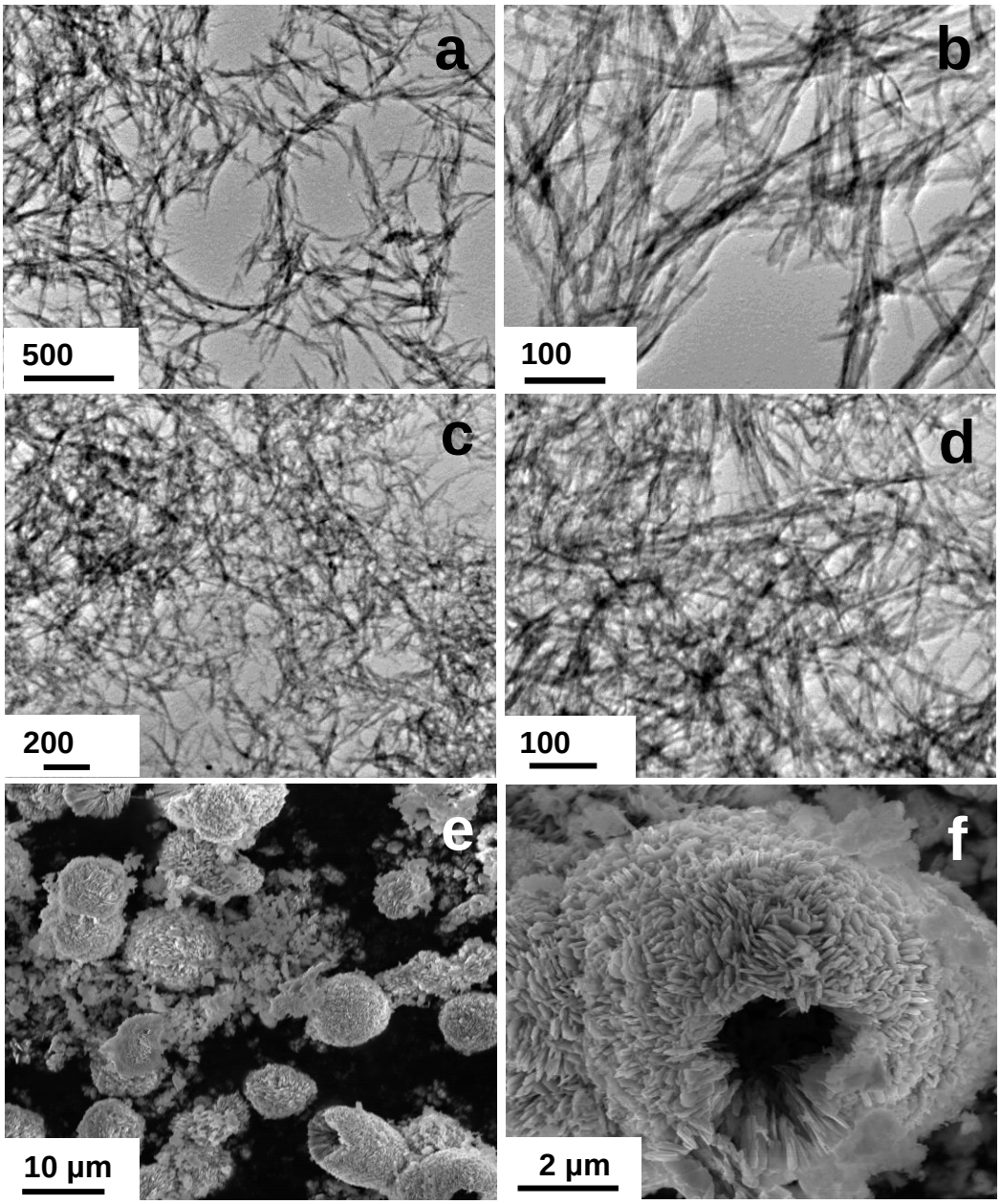

Figure 2. Morphology of mesoporous CuO nanocrystallines with different magnification: (a-b) prepared with $Cu(NO_3)_2$/TOAB=1:1 at room temperature, and (c-d) prepared with $Cu(NO_3)_2$/TOAB=1:2 at room temperature, and (e-f) prepared with $Cu(NO_3)_2$/NaOH=3:1 and 15 mL of ammonia solution at 100 ^{o}C for 24 h.

The morphology of the prepared CuO nanostructures is examined by TEM (Fig.2). As shown in Fig.2a-2b, ribbon-like CuO nanostructures synthesized in the presence of 20 mL TOAB ($Cu(NO_3)_2$/TOAB=1:1) were clearly observed. Observations at high magnification revealed that the width and length of the nanoribbons were about 10-15 nm and 500-600 nm, respectively. Nanoribbon structures were also obtained in sample B in the presence of 40 mL TOAB with average 5-10 nm in width and 200-300 nm in length (Fig.2c-2d). Moreover, adjusting the concentration of TOAB ($Cu(NO_3)_2$/TOAB=2:1) in the reaction mixture did not alter the morphology of CuO significantly (See Supplementary Information, SI-2), although there exist differences among their crystal size and structures. In order to illustrate the effect of CuO morphology on electrochemical property, hydrothermal-synthesized CuO (sample C) is harvested. As shown in Fig.2e-2f, it can be observed that the CuO crystallites self-organized into spherical assemblies or "dandelions" with diameters ranging from 4 to 8 um [29].

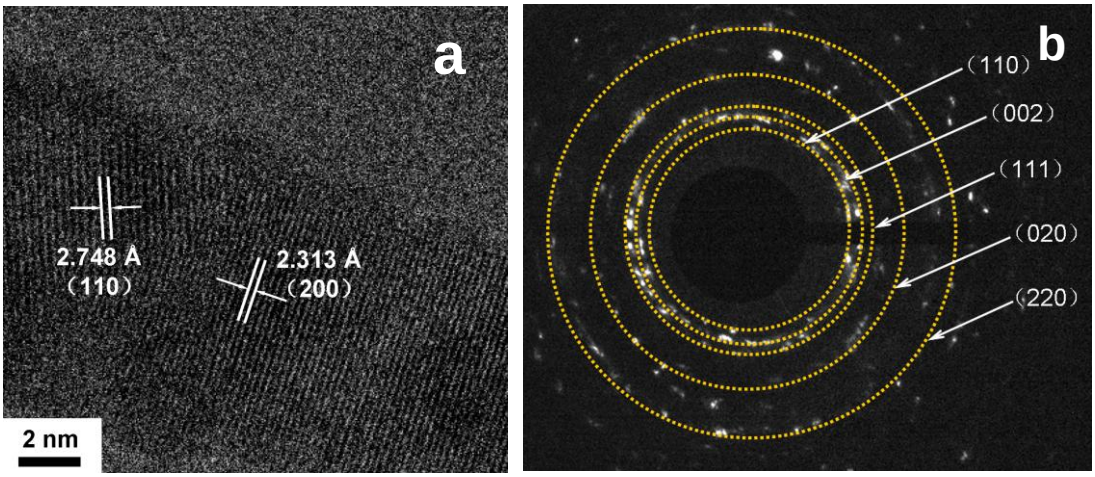

Figure 3. (a) HRTEM images of the as-prepared single CuO nanoribbon (Sample B); (b) SAED pattern of the CuO nanoribbons synthesized by the wet chemical process using 0.05 M $Cu(NO_3)_2$, 0.05 M TOAB, and 1 M NaOH for 1.5 h at room temperature.

Fig.3 presents a typical HRTEM of a single ribbon (sample B) and the SAED pattern (corresponding TEM image was shown in supplementary information, SI-3), taken from a region rich in nanoribbons. In Fig.3a, the clearly visible lattice fringes are indicative of the high crystallinity of the porous skeleton. The interplanar distance of 2.748 Å can be ascribed to the (110) plane of monoclinic CuO, while the interplanar distance of 2.323 Å can be ascribed to the (200) plane, which is well consistent with the XRD results. The SAED pattern of the as prepared CuO crystals indicates that the CuO nanoribbons prepared with $Cu(NO_3)_2$/TOAB=1:2 are actually polycrystalline. The diffraction rings on SAED images match the peaks in XRD pattern, which also proves the monoclinic structure of the prepared CuO nanoribbons.

For the sake of investigating what influence the formation of ribbon-like CuO, experiment without adding TOAB was further carried out, while there was no brownish black precipitate, and the clear, light-blue colored solution remains transparent. Although we could not understand the exact growth mechanism of the ribbon-like CuO and the specific role of TOAB in the reaction, a possible

formation process could be proposed. Firstly, the reaction was dominated by the oriented interconnection of nanoparticles, forming individual $Cu(OH)_2$ nanowires, and then under the action of TOAB, TOA^+ headgroup preferentially binds to the oxygen atom carrying partial negative charge on the $Cu(OH)_2$ surface. In addition, $Cu(OH)_2$ and CuO nanowire bundles were formed by side self-assembly. Finally, continuous crystallization led to the formation of CuO nanoribbons. Previous work has demonstrated that the nanoparticles for nanostructures are usually stabilized by surfactants or polymers, which could modulate the kinetic growth and determine the subsequent morphologies of the final products [32-35]. And when using 40 mL TOAB ($Cu(NO_3)_2$/TOAB=1:2), the products were still CuO nanoribbons, the only difference is that the nanoribbons are narrower and shorter. This is a reasonable deduction, as when the concentration of TOAB increased, thus more TOAB molecules could adsorb on the surface of CuO surface. As the morphology was unchanged, it can be inferred that the TOAB may have acted as a growth-directing agent for the nanostructure formation. On the basis of these observations and analysis, it can be concluded that the CuO nanoparticles spontaneously self-assembled into the nanoribbons via oriented attachment in the presence of TOAB. Thereafter, we could suppose that the existence of TOAB was favorable for the formation of ribbon-like CuO nanostructures.

3.2 FT-IR and thermal properties

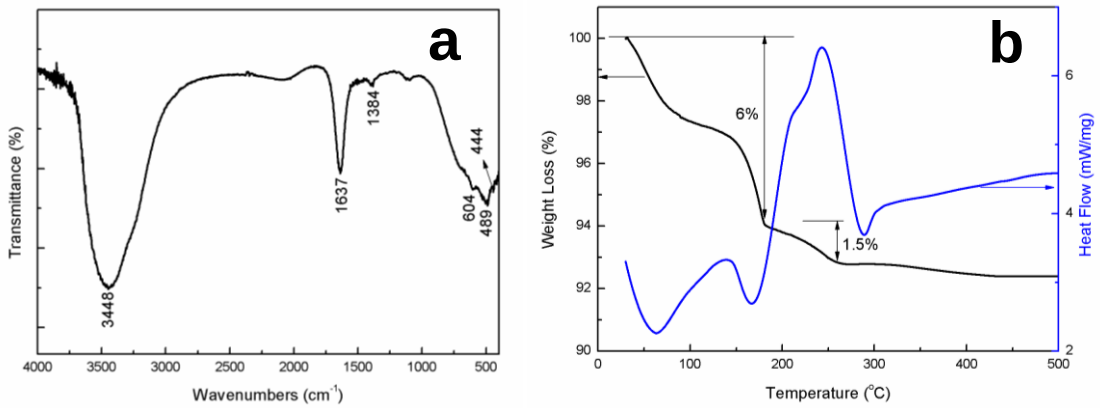

Figure 4. FT-IR spectra (a) and TGA-DSC curves (b) of mesoporous CuO nanoribbions prepared with $Cu(NO_3)_2$/TOAB=1:2 at room temperature.

The FT-IR spectrum was used to investigate the surface properties of the CuO nanostructure (sample B) synthesized at room temperature. As presented in Fig. 4a, the absorption peaks located at the 604, 489, and 444 cm^{-1} are assigned to the Cu-O stretching vibration [36-38], which confirm the formation of CuO nanocrystals. While the broad band centered at 3448 and 1637 cm^{-1} are attributed to the O-H stretching and bending modes of water [39, 40]. The weak bands around 1384 cm^{-1} corresponded to the C–H vibration, indicating few surfactants absorbed on the surface of CuO samples.

The thermal stability of the as-synthesized CuO nanostructure (sample B) was studied by simultaneous DSC and TGA, so as to characterize CuO in terms of a weight change or a phase change between 30 and 500 °C in N_2. The first weight loss of 6% between 50 ^oC and 170 ^oC resulted from the removal of physically absorbed water and chemically bound water. There are two endothermic DSC peaks around 70 °C and 170 ^oC which confirm the evaporation of water, this feature is in good agreement with the TGA results [22, 41]. The temperature range from 170 to 260 °C and this particular weight loss (1.5%) may be ascribed to the loss of the decomposition of few residual surfactants. The sharp exothermic DSC peak around 250 °C is consistent with the decomposition of residual polymer decomposition in as-prepared CuO sample. As no significant weight loss has been observed beyond 400 ^oC in sample B, this result indicates thermal stabilization of the as-prepared CuO.

3.3 Surface area and porosity analysis

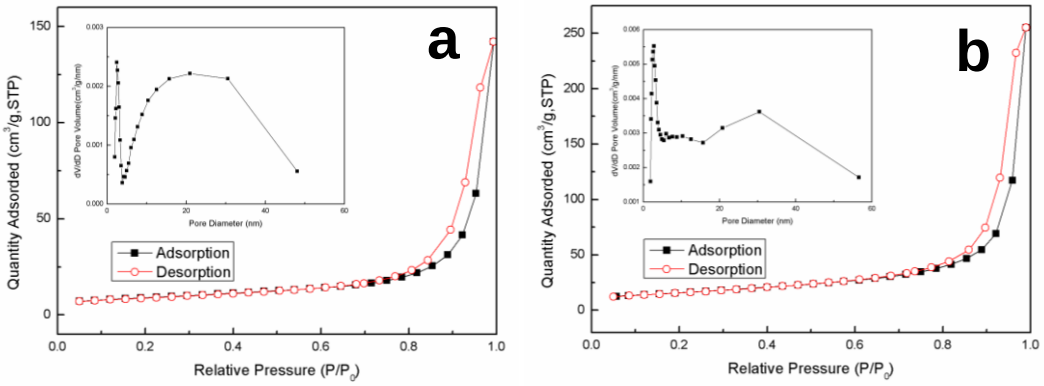

Figure 5. N_2 adsorption-desorption isotherms and its corresponding pore size distribution (inset) of CuO nanoribbons: a) prepared with $Cu(NO_3)_2$/TOAB=1:1 at room temperature, and b) prepared with $Cu(NO_3)_2$/TOAB=1:2 at room temperature.

In order to further examine surface properties of the as-prepared CuO nanostructure, Brunnauer-Emmett-Teller (BET) nitrogen adsorption/desorption measurement was performed. The corresponding nitrogen adsorption/desorption isotherm and pore size distribution curve (inset) of the CuO (Sample A and B) are shown in Fig.5. Moreover, the as-prepared CuO sample with 10 mL TOAB ($Cu(NO_3)_2$/TOAB=2:1) was also investigated, and its N_2 adsorption/desorption isotherms was displayed in supplementary information (SI-4). As shown in Fig.5, the N_2 adsorption/desorption isotherm of the both as-synthesized CuO samples reflected a typical IV sorption behavior with the profile of a hysteresis loop in the high relative pressure (P/P_0) range between 0.7 and 1.0, which indicated that these CuO had a typical mesoporous structure. The BET surface of sample A (Fig.5a) is calculated to be 31.1 m^2/g, while the sample B (Fig.5b) is 56.3 m^2/g, which are higher than that of previous reported CuO nanostructures [42, 43]. From the corresponding Barett-Joyner-Halenda (BJH) pore diameter distribution curve (inset in Fig.5), the CuO nanoribbons (Sample A) exhibit a broad pore size distribution in the range of 2-40 nm, while the sample B (inset in Fig.5b) shows a relatively narrow distribution around 2 and 30 nm. And thus, these results indicate that CuO possessed

amorphous nanostructure, large surface area and moderate pore size distribution. It may provide possibility of efficient transport of electron and ion, leading to an enhancive electrochemical capacity of these materials.

3.4 Electrochemical properties of the mesoporous CuO

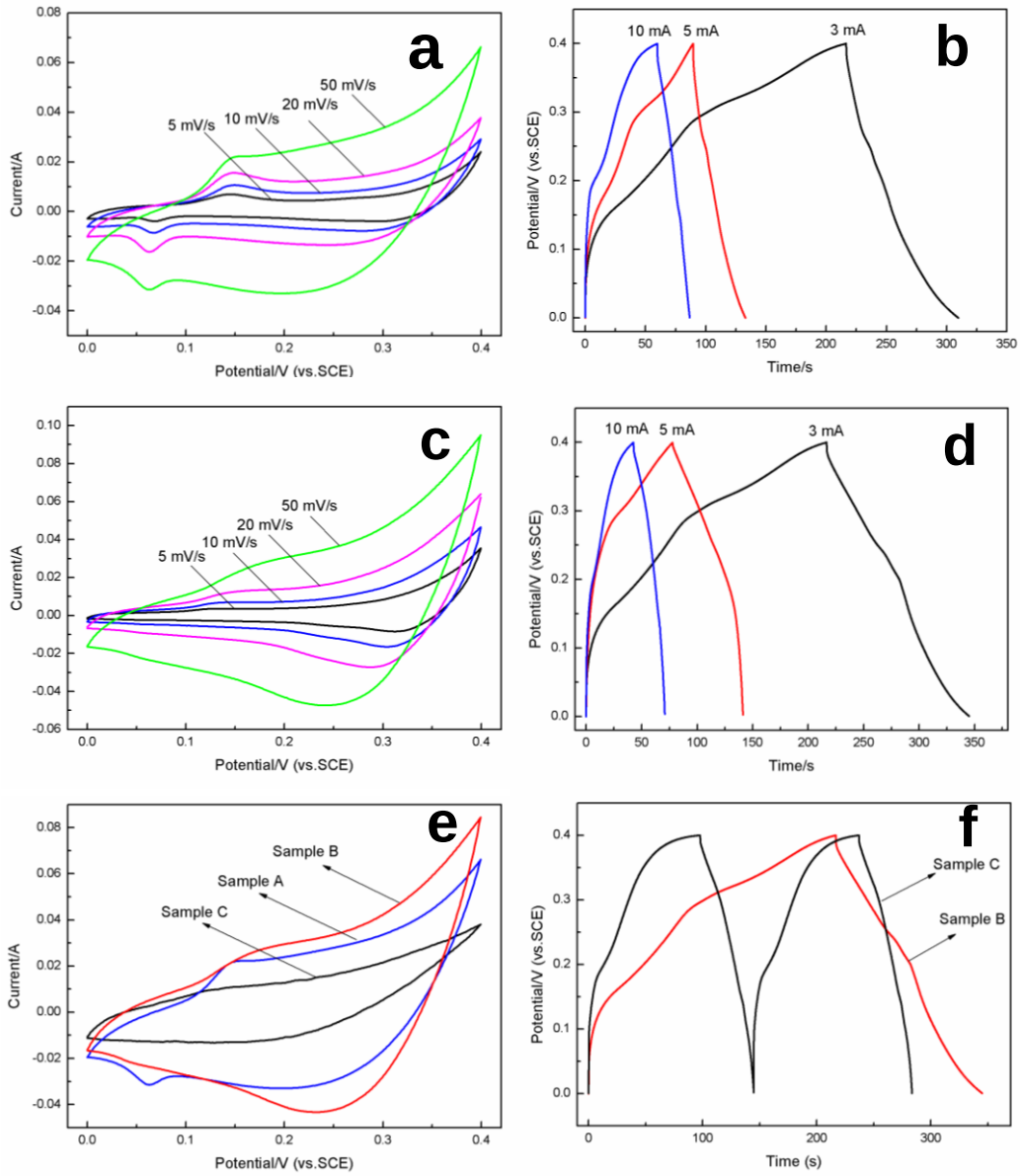

Figure 6. Cyclic voltammograms of CuO nanostructures (Sample A and B) with different scan rate (5, 10, 20 and 50 mV s^{-1}) (a and c) and of different CuO nanostructures (Sample A, B and C) at 50 mV s^{-1} (e) in 6 M KOH aqueous electrolyte; Charge-discharge curves of CuO electrodes (Sample A and B) at different current densities (3, 5 and 10 mA cm^{-2}) (b and d) and of different CuO nanostructures (Sample B and C) at 3 mA cm^{-2} (f); and experimental conditions: Sample A, prepared with $Cu(NO_3)_2$/TOAB=1:1 at room temperature; Sample B, prepared with $Cu(NO_3)_2$/TOAB=1:2 at room temperature; and Sample C, prepared with $Cu(NO_3)_2$/NaOH=3:1 with 15 mL of ammonia solution at 100 ^oC for 24 h.

Capacitor performance of CuO electrode was evaluated with cycle voltammogram (CV) and galvanostatic charge-discharge (GC) measurement in 6 M KOH aqueous solution. Fig.6a and 6c depict the representative CV curves of the prepared mesoporous CuO (sample A and B) measured in a large scan rate range from 5 to 50mV s^{-1} between 0 and 0.4 V. In addition, the CuO prepared with 10 mL TOAB was shown in supplementary information (SI-5a). Clearly, it can be seen that the pseudocapacitance behavior exists in the electrodes which correspond to the redox process between Cu^{2+} and Cu^0 [26, 27, 44, 45]. It can be noted that the shapes of CV curves have no change and the redox-peak position is nearly consistent at different sweep rates. This exhibits stable electrochemical property and higher reversibility of the CuO nanostructures. The specific capacitance of the mesoporous CuO can be calculated from the CV curves according to the following equation

$$C_m = \frac{i}{mv} \qquad (1)$$

where m is the mass of electroactive material CuO, v is the potential sweep rate, and i is the even current response defined by $i=\int_{V_a}^{V_c} i(V)dV/(V_c-V_a)$ (V_a and V_c represent the lowest and highest voltages, respectively) and obtained through integrating the area of the curves in Fig.6a and 6c. The specific capacitance of sample B and C are calculated of 107.6 and 140.7 F g^{-1} with the scan rate of 5 mV s^{-1}, and also the specific capacitance of sample prepared with 10 mL TOAB is 100.1 F g^{-1} (See supplementary information, SI-5a). As shown in Fig.6a and 6c, the specific capacitance of the mesoporous electrode material decrease with increasing scan rates, mainly due to that the redox reactions depend on the insertion/extraction of the alkali ion or protons from the electrolyte. At lower scan rates, the diffusion of ions from the electrolyte could gain access to more available pores of the electrode so as to lead to more insertion/extraction reactions and surface adsorption/desorption of electrolyte cations. Hence, a large specific capacitance can be delivered. When the scan rate increased, the effective interaction between the ions and the electrode and the effective surface adsorption of electrolyte cations would be reduced accordingly. Thus, there is a reduction in specific capacitance.

Additionally, galvanostatic constant current charge-discharge curves at various current densities were performed with a electrochemical window of 0-0.4 V to further examine the power property of the CuO (sample A and B) and representative curves are shown in Fig. 6b and 6d. And the GC curve of the CuO prepared with 10 mL TOAB was also displayed (See supplementary information, SI-5b). The charge curves are almost linear and somewhat mirror symmetrical to their discharge counterparts, suggestive of good electrochemical performance for the mesoporous CuO. Also the specific capacitance of the mesoporous CuO can be calculated from the GC curves using the following equation

$$C_m = \frac{I\Delta t}{\Delta V m} \qquad (2)$$

where I , $\triangle t$, $\triangle V$, and m denote current density, discharge time, potential range in discharge after the IR drop, and the active weight of the electrode material, respectively. The specific capacitance

of the sample B is 137 F g^{-1} which is higher than 104 F g^{-1} of sample A. This result is in agreement with the one obtained from the CV curves in Fig.6a and 6c. According to the results mentioned above, the large capacity of sample B may contribute to the large surface area and moderate pore size distribution. Importantly, it is evident that the maximum specific capacitance of the CuO nanoribbons (sample B) is 137 F g^{-1} at current density of 3 mA cm^{-2} which is little better than the previous reported CuO nanostructures [24-27, 46]. The result shows that the highly mesoporous structure of the electrode facilitates the ions to transfer into the porous structure more easily, making more redox faradic reactions and surface adsorption of electrolyte cations.

And thus, for the sake of investigating the influences of the morphology in the capacitance of electrode materials, the electrochemical properties of the CuO microspheres (sample C) synthesized by hydrothermal route were shown in Fig.6. Fig.6e presents the CV curves of synthesized samples (sample B and C) at scan rate of 50 mV s^{-1}, and the larger area of CV curve for sample B exhibits its specific capacitance is higher than the sample C (CuO microspheres). The galvanostatic charge/discharge behaviors of sample B and C measured in 6 M KOH electrolyte at 3 mA cm^{-2} was displayed in Fig.6f. Sample B with ribbon-like morphology exhibits longer discharge time than sample C (CuO microspheres), the calculated specific capacitance of sample B is 137 F g^{-1} and 85 F g^{-1} of sample C, which indicates the electrochemical properties of CuO can be enhanced through improving morphology of CuO nanocrystals.

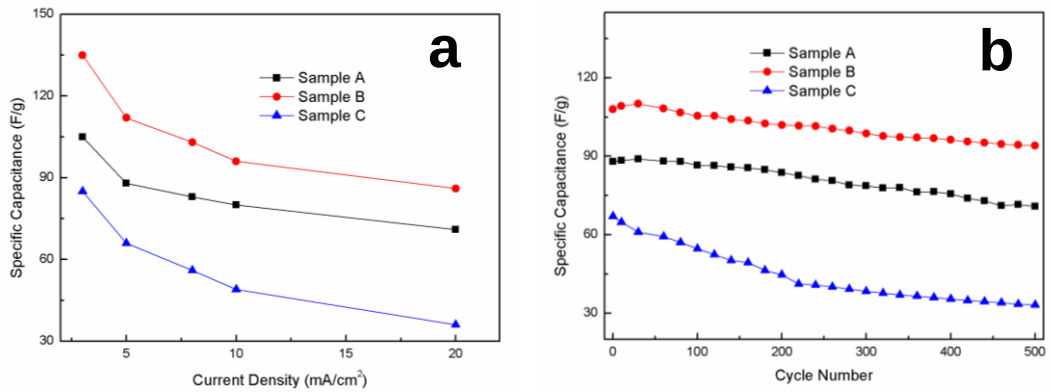

Figure 7. (a) Specific capacitance of CuO nanostructures measured under different current density; (b) cycling performance for different CuO electrodes at a current density of 5 mA cm^{-2} in 6 M KOH; and experimental conditions: Sample A, prepared with $Cu(NO_3)_2$/TOAB=1:1 at room temperature; Sample B, prepared with $Cu(NO_3)_2$/TOAB=1:2 at room temperature; and Sample C, prepared with $Cu(NO_3)_2$/NaOH=3:1 with 15 mL of ammonia solution at 100 ^oC for 24 h.

More importantly, the specific capacitance with different current densities and cycling performance of three samples were shown in Fig.7. The capacitances of the CuO nanostructures decrease slightly with increasing current density from 3 to 20 mA cm^{-2} (Fig.7a). The capacitance retentions are calculated to be 63%, 66%, and 42% for sample A, B, and C, respectively. The good rate capability of sample B can be attributed to the unique mesoporous microstructures and its high specific surface area.

Fig.7b indicates the long-term electrochemical stability of the synthesized mesoporous CuO nanoribbons (sample A and B) and CuO microspheres (sample C) in 6 M KOH electrolyte by charge-discharge cycling at current density of 5 mA cm^{-2} for consecutive 500 cycles. A slight increase in the capacitances was observed during the first 40 cycles for the CuO electrodes (sample A and B), which was attributed to the activation process [47] allowing the trapped cations in the CuO crystal lattice to gradually diffuse out. Such increase in the capacitance during cycling test was not detectable for the sample C of CuO microspheres. This is possibly due to the decrease in capacitance as the electrodes degrade during the cycling charge/discharge processes, which obscured the activation effect [48]. The electrodes of sample B exhibited the best cycling stability among the three electrodes tested, for instance, the capacitance is still 88% of the initial value after 500 charge-discharge processes as compared to 81.4% for sample A and 49.5% for sample C. These results indicate that the mesoporous ribbon-like CuO is a promising candidate as an electrode material for applications in the electrochemical area.

4. CONCLUSIONS

In summary, we have used a simple chemical method at room temperature to synthesize mesoporous CuO nanoribbons. The ribbon-like CuO exhibited comparatively higher specific surface area and porosities. These porous CuO nanoribbons were further tested as pseudocapacitor electrode materials, which were found to exhibit superior performance in terms of specific capacitance and stable cycling performances upon repeated charging/discharging process and had much higher specific capacitances than that of CuO microspheres under the same testing condition. Due to simplicity of the preparation method and their improved electrochemical properties, the mesoporous CuO nanoribbons could be considered as promising electrode materials for the fabrication of electrochemical capacitors.

ACKNOWLEDGEMENTS
The authors gratefully acknowledge the financial supports provided by National Natural Science Foundation of China (Grant no. 51104194), Doctoral Fund of Ministry of Education of China (20110191120014), No. 43 Scientific Research Foundation for the Returned Overseas Chinese Scholars, State Education Ministry and Natural Science Foundation Project of CQ CSTC (CSTS2010BB4058), Fundamental Research Funds for the Central Universities (Project no. CDJZR12248801, Chongqing University, PR China). Dr. Zhang would also like to thank Chongqing University for providing Talent of High Level Scientific Research Fund. Dr. Zhang and Mr. Tan Jian Liang would like to thank National University of Singapore for scholarships and instrumental supports.

References

1. B. E. Conway, *Electrochemical Capacitors: Scientific Fundamentals and Technological Applications*, Kluwer-Plenum Publishing Corp., New work (1999).
2. L. Bao, J. Zang and X. Li, *Nano Lett.*, 11 (2011) 1215.
3. T. Brezesinski, J. Wang, S. H. Tolbert and B. Dunn, *Nat. Mater.*, 9 (2010) 146.

4. Y. Hou, Y. Cheng, T. Hobson and J. Liu, *Nano Lett.*, 10 (2010) 2727.
5. R. B. Rakhi, W. Chen, D. Cha and H. N. Alshareef, *Nano Lett.*, 12 (2012) 2559.
6. H. Wang, C. M. B. Holt, Z. Li, X. Tan, B. S. Amirkhiz, Z. Xu, B. C. Olsen, T. Stephenson and D. Mitlin, *Nano Res.*, 5 (2012) 605.
7. X. He, R. Li, J. Qiu, K. Xie, P. Ling, M. Yu, X. Zhang and M. Zheng, *Carbon*, 50 (2012) 4911.
8. C.-Y. Chen, Z.-Y. Shih, Z. Yang and H.-T. Chang, *J. Power Sources*, 215 (2012) 43.
9. M.-K. Song, S. Cheng, H. Chen, W. Qin, K.-W. Nam, S. Xu, X.-Q. Yang, A. Bongiorno, J. Lee, J. Bai, T. A. Tyson, J. Cho and M. Liu, *Nano Lett.*, 12 (2012) 4416.
10. L. Zhang and G. Shi, *J. Phys. Chem. C*, 115 (2011) 17206.
11. N. Terasawa, K. Mukai and K. Asaka, *J. Mater. Chem.*, 22 (2012) 15104.
12. Y. Murakami, T. Nakamura, X. G. Zhang and Y. Takasu, *J. Alloy. Compd.*, 259 (1997) 196.
13. Y. Q. Zhang, X. H. Xia, J. P. Tu, Y. J. Mai, S. J. Shi, X. L. Wang and C. D. Gu, *J. Power Sources*, 199 (2012) 413.
14. 14 F. Zhang, C. Yuan, X. Lu, L. Zhang, Q. Che and X. Zhang, *J. Power Sources*, 203 (2012) 250.
15. A. Ghosh, E. J. Ra, M. Jin, H.-K. Jeong, T. H. Kim, C. Biswas and Y. H. Lee, *Adv. Funct. Mater.*, 21 (2011) 2541.
16. M. Dong, Y. X. Zhang, H. F. Song, X. Qiu, X. D. Hao, C. P. Liu, Y. Yuan, X. L. Li and J. M. Huang, *Physica E*, 45 (2012) 103.
17. G. Sun, K. Li, C. Sun, Y. Liu and H. He, *Electrochim. Acta*, 55 (2010) 2667.
18. R. Sahay, P. S. Kumar, V. Aravindan, J. Sundaramurthy, W. C. Ling, S. G. Mhaisalkar, S. Ramakrishna and S. Madhavi, *J. Phys. Chem. C*, 116 (2012) 18087.
19. C. W. Zou, J. Wang, F. Liang, W. Xie, L. X. Shao and D. J. Fu, *Curr. Appl. Phys.*, 12 (2012) 1349.
20. V. Dhanasekaran, T. Mahalingam, R. Chandramohan, J.-K. Rhee and J. P. Chu, *Thin Solid Films*, 520 (2012) 6608.
21. J. Liu, J. Jin, Z. Deng, S.-Z. Huang, Z.-Y. Hu, L. Wang, C. Wang, L.-H. Chen, Y. Li, G. Van Tendeloo and B.-L.Su, *J. Colloid. Interf. Sci.*, 384 (2012) 1.
22. I. Singh and R. K. Bedi, *Solid State Sci.*, 13 (2011) 2011.
23. L. Zhang, R. Liu and H. Yang, *Physica E*, 44 (2012) 1592.
24. V. D. Patake, S. S. Joshi, C. D. Lokhande and O.-S. Joo, *Mater. Chem. Phys.*, 114 (2009) 6.
25. D. P. Dubal, D. S. Dhawale, R. R. Salunkhe, V. S. Jamdade and C. D. Lokhande, *J. Alloy. Compd.*, 492 (2010) 26.
26. H. Zhang and M. Zhang, *Mater. Chem. Phys.*, 108 (2008) 184.
27. H. Zhang, J. Feng and M. Zhang, *Mater. Res. Bull.*, 43 (2008) 3221.
28. G. Wang, J. Huang, S. Chen, Y. Gao and D. Cao, *J. Power Sources*, 196 (2011) 5756.
29. B. Liu and H. C. Zeng, *J. Am. Chem. Soc.*, 126 (2004) 8124.
30. Y. Chang and H. C. Zeng, *Cryst. Growth. Des.*, 4 (2004) 397.
31. M. S. Hassan, T. Amna, O. B. Yang, M. H. El-Newehy, S. S. Al-Deyab and M.-S. Khil, *Colloid Surface. B.*, 97 (2012) 201.
32. H. Colfen and S. Mann, *Angew. Chem. Int. Edit.*, 42 (2003) 2350.
33. H. Colfen and M. Antonietti, *Angew. Chem. Int. Edit.*, 44 (2005) 5576.
34. Y. Peng, A. W. Xu, B. Deng, M. Antonietti and H. Colfen, *J. Phys. Chem. B*, 110 (2006) 2988.
35. Y. Li, X.-Y. Yang, J. Rooke, G. van Tendeloo and B.-L. Su, *J. Colloid Interf. Sci.*, 348 (2010) 303.
36. M. Faisal, S. B. Khan, M. M. Rahman, A. Jamal and A. Umar, *Mater. Lett.*, 65 (2011) 1400.
37. Y. G. Zhang, S. T. Wang, X. B. Li, L. Y. Chen, Y. T. Qian and Z. D. Zhang, *J. Cryst. Growth*, 291 (2006) 196.
38. S. C. Vanithakumari, S. L. Shinde and K. K. Nanda, Mater. *Sci. Eng. B-Adv.*, 176 (2011) 669.
39. X. Liu, Z. Li, Q. Zhang, F. Li and T. Kong, *Mater. Lett.*, 72 (2012) 49.
40. J. Xia, H. Li, Z. Luo, H. Shi, K. Wang, H. Shu and Y. Yan, *J. Phys. Chem. Solids*, 70 (2009) 1461.
41. M. Srivastava, A. K. Ojha, S. Chaubey, P. K. Sharma and A. C. Pandey, *J. Alloy Compd.*, 494 (2010) 275.

42. H. Xu, G. Zhu, D. Zheng, C. Xi, X. Xu and X. Shen, *J. Colloid Interf. Sci.*, 383 (2012) 75.
43. L. Xu, S. Sithambaram, Y. Zhang, C.-H. Chen, L. Jin, R. Joesten and S. L. Suib, *Chem. Mater.*, 21 (2009) 1253.
44. J. Y. Xiang, J. P. Tu, J. Zhang, J. Zhong, D. Zhang and J. P. Cheng, *Electrochem. Commun.*, 12 (2010) 1103.
45. S. Venkatachalam, H. Zhu, C. Masarapu, K. Hung, Z. Liu, K. Suenaga and B. Wei, *ACS NANO*, 3 (2009) 2177.
46. D.-W. Kim, K.-Y. Rhee and S.-J. Park, *J. Alloy Compd.*, 530 (2012) 6.
47. C. Yuan, X. Zhang, L. Su, B. Gao and L. Shen, *J. Mater. Chem.*, 19 (2009) 5772.
48. X. Zhang, W. Shi, J. Zhu, D. J. Kharistal, W. Zhao, B. S. Lalia, H. H. Hng and Q. Yan, *ACS NANO*, 5 (2011) 2013

Supplementary Information:

SI-1. XRD patterns of mesoporous CuO nanocrystallines prepared with 10 mL TOAB （ $Cu(NO_3)_2$/TOAB=2:1）at room temperature.

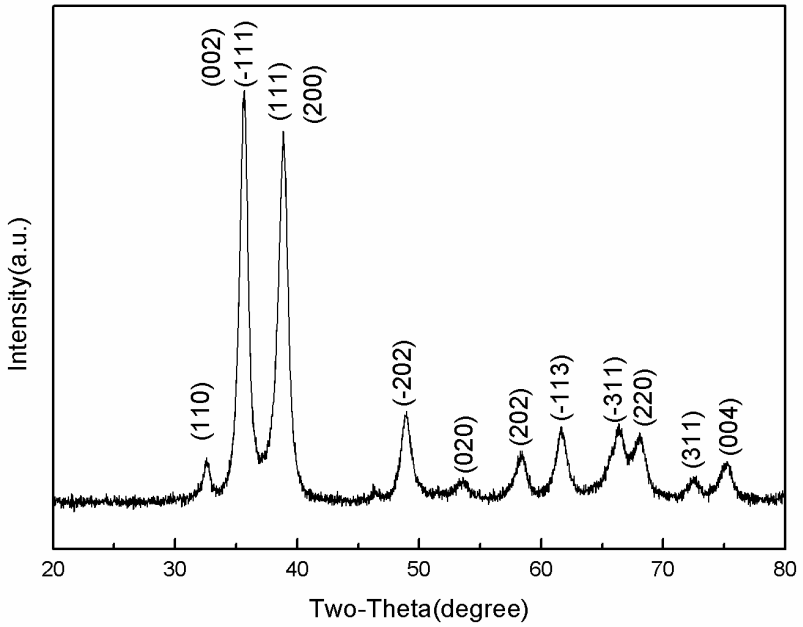

SI-2. Morphology of mesoporous CuO nanocrystallines prepared with 10 mL TOAB （ $Cu(NO_3)_2$/TOAB=2:1）at room temperature with different magnification.

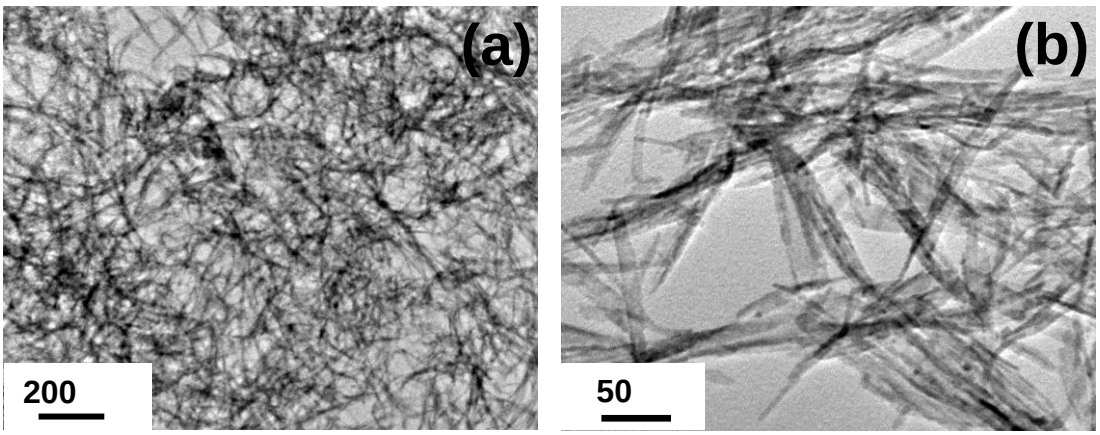

SI-3. The corresponding TEM image of the CuO nanoribbons for the SAED pattern (Fig.3b).

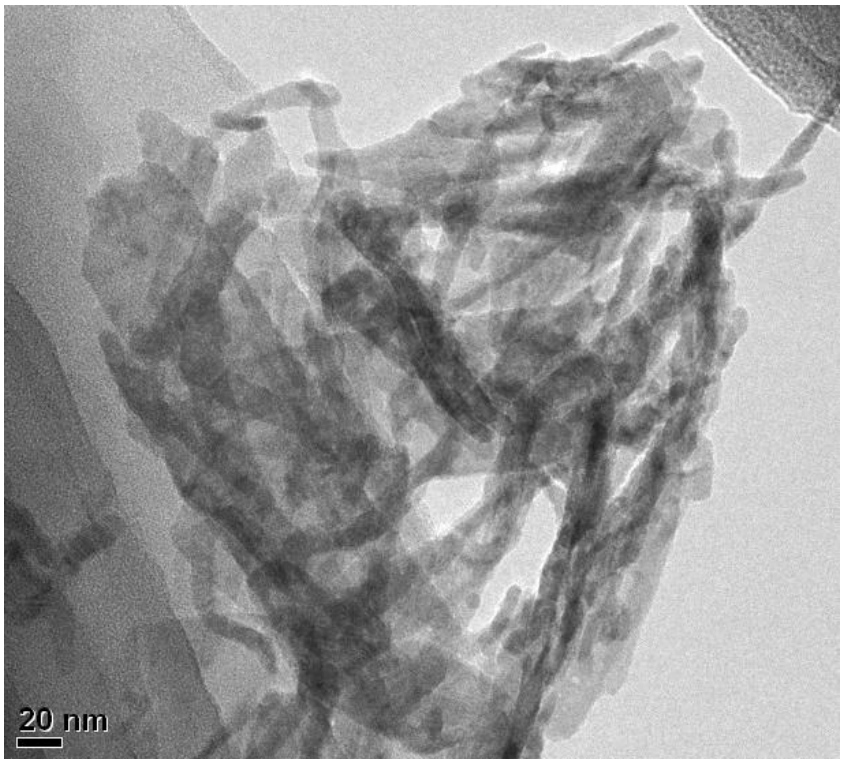

SI-4. N_2 adsorption-desorption isotherms distribution of CuO nanoribbons prepared with 10 mL TOAB ($Cu(NO_3)_2$/TOAB=2:1) at room temperature.

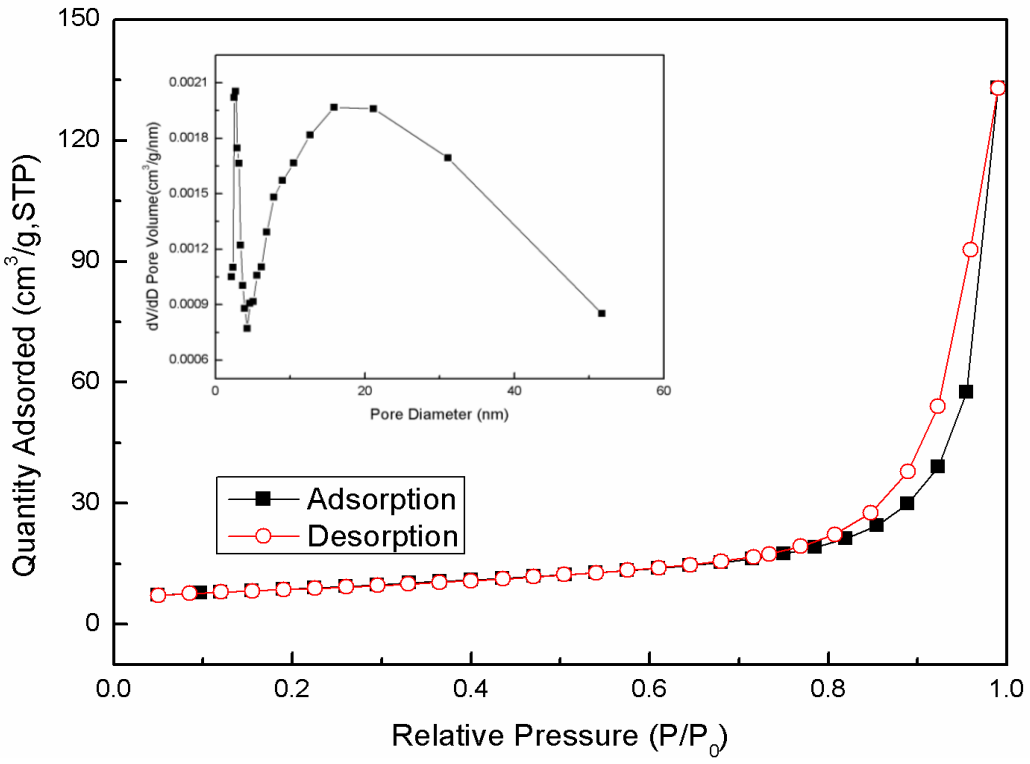

SI-5. Cyclic voltammograms (a) and Charge-discharge curves (b) of CuO nanoribbons prepared with 10 mL TOAB ($Cu(NO_3)_2$/TOAB=2:1) at room temperature.